Grid-Voltage Sensorless Predictive Current Control of Three-Phase PWM Rectifier With Fast Dynamic Response and High Accuracy

Chunjie LI, Jianing HU, and Mingwei ZHAO

***Abstract*—To improve pure integral calculations with integral drift and dc bias, and poor dynamic response under conventional direct power control, a grid-voltage sensorless predictive current control strategy of three-phase PWM rectifier is proposed. In the voltage sensorless control algorithm, an improved virtual flux observer is constructed by introducing bandstop filter feedback to solve the dc bias. Moreover, to address the inaccurate voltage-vector selection algorithm in the two-step prediction, Lagrange interpolation is introduced to make the predictive current more accurate. Experimental results verify that the three-phase PWM rectifier with the proposed strategy can achieve high power factor, high prediction accuracy and improve dynamic performance of the system.**

***Index Terms*—Lagrange interpolation, predictive current control, three phase PWM rectifier, virtual flux observer, voltage sensorless.**

I. Introduction

FOR specific applications, such as electric vehicles and aerospace industries, power electronic converters with safety, reliability and high power density have been attracting more and more attention. A three-phase PWM rectifier can be a good choice for power electronic equipments with medium and high power levels [1]. When power electronic conversion systems are operated in complex working condition and harsh environment, sensor failures can occur, leading to degradation of the system performance or even a system breakdown [2]. In order to improve the safety and reliability, a three-phase PWM rectifier without grid voltage sensors is presented. In addition, the PWM rectifier has high power factor [3], [4]. In the specific applications, the control performance needs further improvement.

To address the problems of weak dynamic response and wide power ripples in the traditional vector control of the three-phase rectifier [5], [6], model predictive control (MPC) is first presented and applied to the rectifier [7], which is used to suppress power ripples. However, the power prediction precision requires improvement. Generally, direct power control is often combined with predictive control to achieve better power control. A model predictive direct power control (MPDPC) with duty cycle control [8], [9] is presented to reduce the average switching frequency and the instantaneous power pulsation. In [10], the method that forcing the two non-zero voltage vectors to alternate is used to improve the power tracking accuracy, but the power is still subject to large perturbation.

In order to achieve lightweight and miniaturization of power electronics [11], a grid-side voltage sensorless is used, however, the MPDPC is dependent on the grid's voltage and current parameters [12], [13]. Then, a voltage observer is introduced and used instead of the sensor hardware.

Most voltage observers adopt virtual flux-oriented control [14], in which, the traditional virtual flux is found by performing a pure integration calculation directly on the voltage vector, but this leads to integration drift and dc bias. A first-order low-pass (FOLP) filter [15] is used instead of pure integration calculation, which can not choose the initial value of the integral. However, it exists amplitude error and phase error [16]. To reduce the errors, the compensation gain is added in the FOLP filter is presented in [17], [18], and the cross-compensation is proposed in [19]−[21], meanwhile, both of them can eliminate the dc bias problem. To solve the defects of traditional virtual flux, the virtual flux observer using a second-order generalized integrator is proposed in [22]−[25], which presents satisfactory control under balanced and unbalanced grid-voltage, but exits static error while tracking the AC signal. To improve observation precision, the virtual flux observer using a second-order low-pass (SOLP) filter is presented in [26]−[28], which can effectively solve the integration offset. However, the SOLP filter can not eliminate dc component in the flux observer. A second-order bandpass filter added in the SOLP filter [29] is presented, which can extract the fundamental signal from the virtual flux to improve the accuracy of prediction. Therefore, there is room for improvement in the performance of the voltage-flux observer.

On the basis of the above analysis, this paper proposes an

Manuscript received December 14, 2022; revised February 24, 2023 and May 11, 2023; accepted June 11, 2023. Date of publication September 30, 2023; date of current version September 5, 2023. This work was supported in part by the China National Science Foundation under Grant 51707085, in part by Xuzhou Science and Technology Project under Grant KC22006, and in part by Graduate Research and Practice Innovation Program of Jiangsu Normal University under Grant 2022XKT0153. *(Corresponding author: Mingwei Zhao.)*

C. Li and J. Hu are with the Electrical Engineering Department, Jiangsu Normal University, Xuzhou 221116, China (e-mail: lcj_85@163.com; 2020211632@jsnu.edu.cn).

M. Zhao is with the Electrical Engineering Department, Jiangsu Normal University, Xuzhou 221116, China and also with the School of Mechatronic Engineering and Automation, Shanghai University, Shanghai 200444, China (e-mail: xznu_zmw@jsnu.edu.cn).

Digital Object Identifier 10.24295/CPSSTPEA.2023.00037

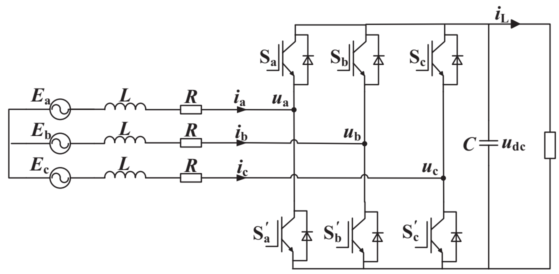

Fig. 1. Main circuit of PWM rectifier.

improved virtual-flux model predictive current control (VF-MPCC) strategy. The strategy introduces a bandstop filter feedback to the SOLP filter-based virtual flux observer. By suppressing the dc component of the reconstructed voltage vector, the voltage estimation accuracy can be improved substantially. Then, with the instantaneous power theory, an objective cost function is established to minimize the power error, and the target prediction current is then derived. To address the problem of signal lag, a two-step predictive current method is used to compensate, while Lagrange interpolation is introduced to correct the predicted voltage values and improve the prediction accuracy. Finally, the improved VF-MPCC is experimentally validated against virtual flux-based direct power control (VF-DPC). The experimental results are verified that the control performance with the improved VF-MPCC is improved from power ripple, dynamic response and prediction accuracy.

The paper structure is presented. Section II depicts the PWM rectifier's mathematical model, the grid voltage estimation, and the modeling of an improved virtual flux observer. Section III analyzes predictive control strategy for PWM rectifier, including the model predictive current control strategy and new voltage vector prediction. Section IV presents and analyzes all experimental results. Finally, Section V draws conclusions.

II. System Modelling With Grid Voltage Sensor

A. Model of PWM Rectifier

A three-phase PWM rectifier circuit is shown in Fig. 1. E_a, E_b, and E_c are the ideal grid voltages; R and L are the grid-side equivalent resistance and filter inductance; i_a, i_b, and i_c are the grid-side phase currents; u_a, u_b, and u_c are the AC-side voltages; C is the DC-side capacitor; i_L is the DC-side load current; R_L is the DC-side load resistance; and u_{dc} is the DC-side bus voltage.

Based on the transformation principle of the two-phase fixed coordinate system, the mathematical model of the three-phase PWM rectifier on the α-β axis is obtained as [19]:

$$\begin{cases} L\dfrac{\mathrm{d}i_\alpha}{\mathrm{d}t} = E_\alpha - Ri_\alpha - V_\alpha \\ L\dfrac{\mathrm{d}i_\beta}{\mathrm{d}t} = E_\beta - Ri_\beta - V_\beta \\ C\dfrac{\mathrm{d}u_{\mathrm{dc}}}{\mathrm{d}t} = S_\alpha i_\alpha + S_\beta i_\beta - i_{\mathrm{L}} \end{cases} \tag{1}$$

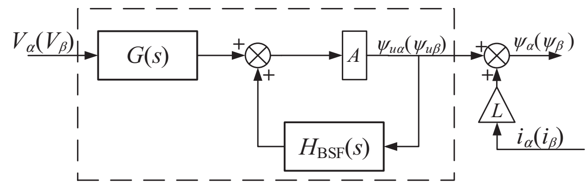

Fig. 2. Structure of the improved virtual flux observer.

where E_α, E_β, i_α, and i_β are the components of the network-side voltage and current in the α and β axes, respectively; V_α and V_β are the components of the AC-side voltage in the α and β axes, respectively; S_α and S_β are the values of the switching function in the two-phase fixed coordinate system, respectively.

To eliminate the net-side three-phase voltage sensor, the virtual flux concept was presented in [30]. Since the virtual flux vector ψ lags the grid-side voltage vector by 90°, it can get the virtual flux expression by integrating the grid-side voltage vector, neglecting the internal resistance R, as follows:

$$\begin{cases} \psi_\alpha = \int E_\alpha \mathrm{d}t = Li_\alpha + \int V_\alpha \mathrm{d}t \\ \psi_\beta = \int E_\beta \mathrm{d}t = Li_\beta + \int V_\beta \mathrm{d}t \end{cases} \tag{2}$$

B. Grid Voltage Estimation

According to (2) and the relation between the flux vectors ψ_α and ψ_β, it can be obtained as:

$$\begin{cases} \sin\theta = \dfrac{\psi_\beta}{\sqrt{\psi_\alpha^{\ 2} + \psi_\beta^{\ 2}}} \\ \cos\theta = \dfrac{\psi_\alpha}{\sqrt{\psi_\alpha^{\ 2} + \psi_\beta^{\ 2}}} \end{cases} \tag{3}$$

$$\begin{bmatrix} E_\alpha \\ E_\beta \end{bmatrix} = \omega \begin{bmatrix} -\psi_\beta \\ \psi_\alpha \end{bmatrix} \tag{4}$$

From (3) and (4), it can be obtained the angle and amplitude of the grid voltage, which are related to magnetic flux ψ. Therefore, the accuracy of the voltage vector estimation depends on the virtual flux.

C. Virtual Flux Observer Model With Bandstop Filter Feedback

Traditional virtual flux observers do a straightforward calculation of the AC side voltage components' pure integration in the α-β coordinate system. However, the calculation's results are significantly impacted by the selection of the integration's beginning value. It is likely to cause integration drift, output saturation and to introduce dc components causing dc bias. To reduce the effect of the above-mentioned problems, this paper proposes a virtual flux observer with the introduction of a feedback link of a bandstop filter to achieve a pure integration effect and to enable the suppression of the dc component in the reconstructed voltage. Its structure diagram is shown in Fig. 2.

The transfer function $G(s)$ of the SOLP filter and the transfer function of the bandstop filter $H_{\mathrm{BSF}}(s)$ in Fig. 2, are specified as follows:

$$G(s)=\frac{k\omega_c}{s^2+k\omega_c s+\omega_c^2}$$
$$H_{\mathrm{BSF}}(s)=\frac{s^2+\omega_c^2}{s^2+2\xi\omega_c s+\omega_c^2} \tag{5}$$

where k is the gain of the SOLP filter, here taken as 2, ω_c is equal to the fundamental angular frequency ω [27], and ξ is the damping factor. A is taken as the reciprocal of the output amplitude for the transfer function $G(s)$.

$$A=\frac{1}{|G(s)V(\alpha)|} \tag{6}$$

From Fig. 2, it can be deduced as follows:

$$\psi_{u\alpha}(s)=[V_\alpha(s)G(s)+H_{\mathrm{BSF}}(s)\psi_{u\alpha}(s)]A \tag{7}$$

Substituting the transfer function $G(s)$ and $H_{\mathrm{BSF}}(s)$ to (7), it can be written as:

$$\psi_{u\alpha}(s)=\frac{2\omega_c}{s^2+2\omega_c s+\omega_c^2}\frac{A(s^2+2\xi\omega_c s+\omega_c^2)}{(1-A)s^2+2\xi\omega_c s+(1-A)\omega_c^2}V_\alpha(s) \tag{8}$$

When ξ is equal to one, the transfer function of the virtual flux observer from (8) can be written as：

$$\psi_{u\alpha}(s)=\frac{2A\omega_c}{(1-A)s^2+2\omega_c s+(1-A)\omega_c^2}V_\alpha(s) \tag{9}$$

Then from (9), the improved transfer function of SOLP filter can be expressed as:

$$G_1(s)=\frac{2A\omega_c}{(1-A)s^2+2\omega_c s+(1-A)\omega_c^2} \tag{10}$$

And a frequency characteristic analysis of (10), substituting $s=\mathrm{j}\omega$ into (9), is shown as follows:

$$G_1(\mathrm{j}\omega)=\frac{2A\omega}{(1-A)(\mathrm{j}\omega)^2+2\omega\mathrm{j}\omega+(1-A)\omega^2}=A\frac{1}{\mathrm{j}\omega} \tag{11}$$

From (11), the improved virtual flux can achieve the effect of pure integration, and solve the problem of integration offset caused by improperly chosen initial integration value. A comparison between the improved virtual flux and the output flux calculated by pure integration is shown in Fig. 3. From Fig. 3, it can be found that, the virtual flux calculated by the improved virtual flux algorithm fluctuates along the zero axis and its average value over a period is approximately 0.

Fig. 4 shows the Bode diagram and virtual flux circle obtained by the FOLP filter, the SOLP filter and the proposed method respectively. From Fig. 4(a) and (b), at the fundamental frequency of 314 rad/s, the phase characteristics of the improved VF and the normal SOLP are same, and the amplitude characteristic curve of the improved VF is shifted downwards. From Fig. 4(c), it can be seen that the flux circle starts at the centre of the flux circle, but with the FOLP filter control, the flux circle obtained is not stable and the startup overshoot is extremely large. Compared with the SOLP filter

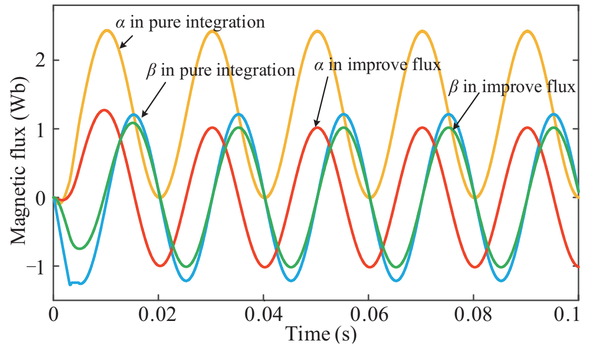

Fig. 3. Comparison between pure integration virtual flux and improved virtual flux.

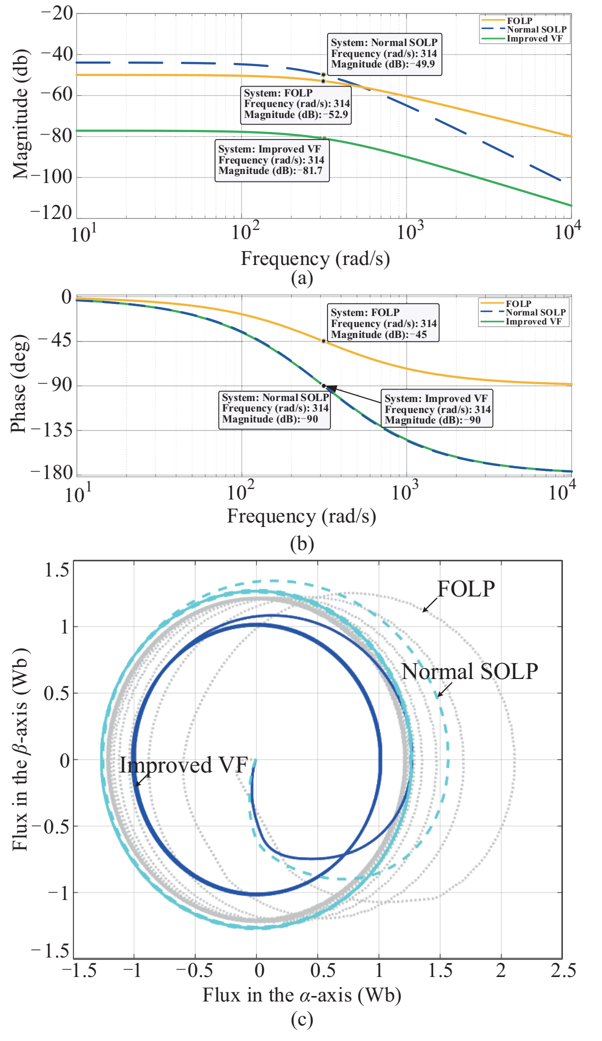

Fig. 4. The Bode diagram and virtual flux circle. (a) Magnitude characteristic. (b) Phase characteristic. (c) Virtual flux trajectory diagram for the three methods.

control, the initial DC component is smaller with the proposed method.

III. Predictive Control Strategy

A. Predictive Current Control Strategy

Following the instantaneous power theory [25], the instantaneous power calculation expression can be obtained as:

$$\begin{cases} P = (\psi_\alpha i_\beta - \psi_\beta i_\alpha)\omega \\ Q = (\psi_\alpha i_\alpha + \psi_\beta i_\beta)\omega \end{cases} \tag{12}$$

Substituting (4) into (12) can be gotten:

$$\begin{bmatrix} P \\ Q \end{bmatrix} = \begin{bmatrix} E_\alpha & E_\beta \\ E_\beta & -E_\alpha \end{bmatrix} \begin{bmatrix} i_\alpha \\ i_\beta \end{bmatrix} \tag{13}$$

Since the sample period is substantially shorter than the power grid's fundamental wave period, the internal resistance R can be neglected, the current discretization from (1) at the moment $(k+1)$ can be obtained as:

$$\begin{cases} i_\alpha(k+1) = \dfrac{T_s}{L}\left[E_\alpha(k) - V_\alpha(k)\right] + i_\alpha(k) \\ i_\beta(k+1) = \dfrac{T_s}{L}\left[E_\beta(k) - V_\beta(k)\right] + i_\beta(k) \end{cases} \tag{14}$$

Taking the derivative of (13), after its discretization, the predicted value of the instantaneous power at $(k+1)$th instant is obtained as [28]:

$$\begin{cases} P(k+1) = -\omega T_s Q + E_\alpha i_\alpha(k+1) + E_\beta i_\beta(k+1) \\ Q(k+1) = \omega T_s P + E_\beta i_\alpha(k+1) - E_\alpha i_\beta(k+1) \end{cases} \tag{15}$$

To achieve the minimum instantaneous power error, the objective cost function is defined as:

$$g = [(P_{\text{ref}} - P(k+1)]^2 + [(Q_{\text{ref}} - Q(k+1)]^2 \tag{16}$$

When $\partial g / \partial i_\alpha(k+1) = 0$ and $\partial g / \partial i_\beta(k+1) = 0$, it can realize the minimality of the instantaneous power error. Then, the current prediction at $(k+1)$th instant can be obtained as:

$$\begin{bmatrix} i_\alpha(k+1) \\ i_\beta(k+1) \end{bmatrix} = B \begin{bmatrix} E_\alpha(k) & E_\beta(k) \\ E_\beta(k) & -E_\alpha(k) \end{bmatrix} \begin{bmatrix} P_{\text{ref}} + \omega T_s Q \\ Q_{\text{ref}} - \omega T_s P \end{bmatrix} \tag{17}$$

Where

$$B = \frac{1}{\omega^2({\psi_\alpha}^2 + {\psi_\beta}^2)} \tag{18}$$

Substituting (17) into (14) yields:

$$\begin{cases} V_\alpha(k) = -\dfrac{L}{T_s}\left[i_\alpha(k+1) - i_\alpha(k)\right] + E_\alpha(k) \\ V_\beta(k) = -\dfrac{L}{T_s}\left[i_\beta(k+1) - i_\beta(k)\right] + E_\beta(k) \end{cases} \tag{19}$$

However, in actual systems, the signal processing cannot be finished instantly and may cause a signal lag of one switching cycle. For compensation of this signal lag, a two-step prediction method is used, predicting one more beat backward to the $(k+2)$ moment to achieve compensation. A second derivative and discretization of (13) can be written as:

$$\begin{cases} P(k+2) = -\omega T_s Q(k+1) + E_\alpha(k+1) i_\alpha(k+2) + \\ \qquad E_\beta(k+1) i_\beta(k+2) \\ Q(k+2) = \omega T_s P(k+1) + E_\beta(k+1) i_\alpha(k+2) - \\ \qquad E_\alpha(k+1) i_\beta(k+2) \end{cases} \tag{20}$$

At this point, the objective cost function can be redefined as:

$$g = [(P_{\text{ref}} - P(k+2)]^2 + [(Q_{\text{ref}} - Q(k+2)]^2 \tag{21}$$

Making $\partial g / \partial i_\alpha(k+2) = 0$ and $\partial g / \partial i_\beta(k+2) = 0$, the instantaneous power error can be minimized. Then, the current prediction at $(k+2)$th instant can be found, as follows:

$$\begin{bmatrix} i_\alpha(k+2) \\ i_\beta(k+2) \end{bmatrix} = B_1 \begin{bmatrix} E_\alpha(k+1) & E_\beta(k+1) \\ E_\beta(k+1) & -E_\alpha(k+1) \end{bmatrix} \begin{bmatrix} P_{\text{ref}} + \omega T_s Q(k+1) \\ Q_{\text{ref}} - \omega T_s P(k+1) \end{bmatrix} \tag{22}$$

Where

$$B_1 = \frac{1}{\omega^2[\psi_\alpha(k+1)^2 + \psi_\beta(k+1)^2]} \tag{23}$$

At $(k+1)$th instant, the new voltage vector value is obtained as:

$$\begin{cases} V_\alpha(k+1) = -\dfrac{L}{T_s}\left[i_\alpha(k+2) - i_\alpha(k+1)\right] + E_\alpha(k+1) \\ V_\beta(k+1) = -\dfrac{L}{T_s}\left[i_\beta(k+2) - i_\beta(k+1)\right] + E_\beta(k+1) \end{cases} \tag{24}$$

B. New Voltage Vector Prediction

Since the grid voltage vector values at the moment $(k+1)$ are not directly available, and in conventional predictive control, it is usually considered that $E(k+1) \approx E(k)$. However, when the grid-side voltage period differs from the sampling period by a small amount, this can introduce large errors. The paper proposes using Lagrange interpolation in rectifiers to predict the grid voltage vector E, such that $E(k+1/2) \approx E(k+1)$, to improve the accuracy of the voltage vector. The mathematical formula of Lagrange interpolation is:

$$f(x) = \frac{(x-x_2)(x-x_3)}{(x_1-x_2)(x_1-x_3)} f(x_1) + \frac{(x-x_1)(x-x_3)}{(x_2-x_1)(x_2-x_3)} f(x_2) + \frac{(x-x_1)(x-x_2)}{(x_3-x_1)(x_3-x_2)} f(x_3) \tag{25}$$

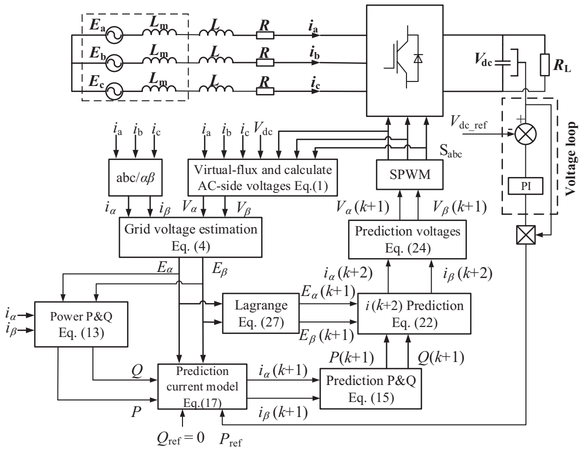

Fig. 5. Control diagram of the improved VF-MPCC.

Where $x_1 = k - 2,\ x_2 = k - 1, x_3 = k$.

Making $x = k + 1/2$, the function at $(k + 1/2)$th instant can be described as:

$$f(k+1/2) = 0.375f(k-2) - 1.25f(k-1) + 1.875f(k) \quad (26)$$

Then the grid vector value at $(k + 1/2)$th instant can be represented as:

$$E(k+1/2) = 0.375E(k-2) - 1.25E(k-1) + 1.875E(k) \quad (27)$$

Substituting (27) into (22), it can be obtained a more accurate voltage vector value at the moment $(k + 1)$, as follows:

$$\begin{cases} V_\alpha(k+1) = -\dfrac{L}{T_s}\left[i_\alpha(k+2) - i_\alpha(k+1)\right] + E_\alpha(k+1/2) \\ V_\beta(k+1) = -\dfrac{L}{T_s}\left[i_\beta(k+2) - i_\beta(k+1)\right] + E_\beta(k+1/2) \end{cases} \quad (28)$$

From previous analysis, it can be obtained the control diagram of the improved VF-MPCC based on Lagrange interpolation for PWM rectifier, as shown in Fig. 5.

IV. Experiment Results

To verify the improved VF-MPCC method, experimental results are presented by using the Typhoon semi-physical experimental platform. For a comprehensive comparison of rectifier control performance, the experimental comparison between the VF-DPC and the modified VF-MPCC with the same parameters are given. The rectifier's experimental parameters are displayed in Table I.

The experimental waveforms of PWM rectifier with VF-DPC and improved VF-MPCC under steady-state are shown in Fig. 6. Phase-A voltage and current, DC-link output voltage and current with VF-DPC are presented in Fig. 6(a), in which, grid side voltage and input current are basically in phase, and the output voltage is stable at 620 V. Phase-A voltage and current, DC-link output voltage and current with improved VF-MPCC are presented in Fig. 6(b), it can be seen that the grid-side voltage and current remain in phase. The THD waveform of the grid current from Fig. 6(a) is shown in Fig. 6(c), which is 4.14% measured by power analyzer. The THD waveform of the grid current from Fig. 6(b) is shown in Fig. 6(d), which is 1.34%. Compared with Fig. 6(a) and (c) with VF-DPC, the grid current THD with improved VF-MPCC is lower.

TABLE I
MAIN EXPERIMENTAL PARAMETERS

Symbol	Parameters	Values
U_a	Grid voltage	220 V_{rms}
f	Rated frequency	50 Hz
L	Filter inductance	10 mH
C	DC-link capacitor	470 μF
R	Load-side resistor	100 Ω
V_{dc}	Dc-link voltage	620 V
P	Rated output power	4 kW
f_s	Switching frequency	20 kHz

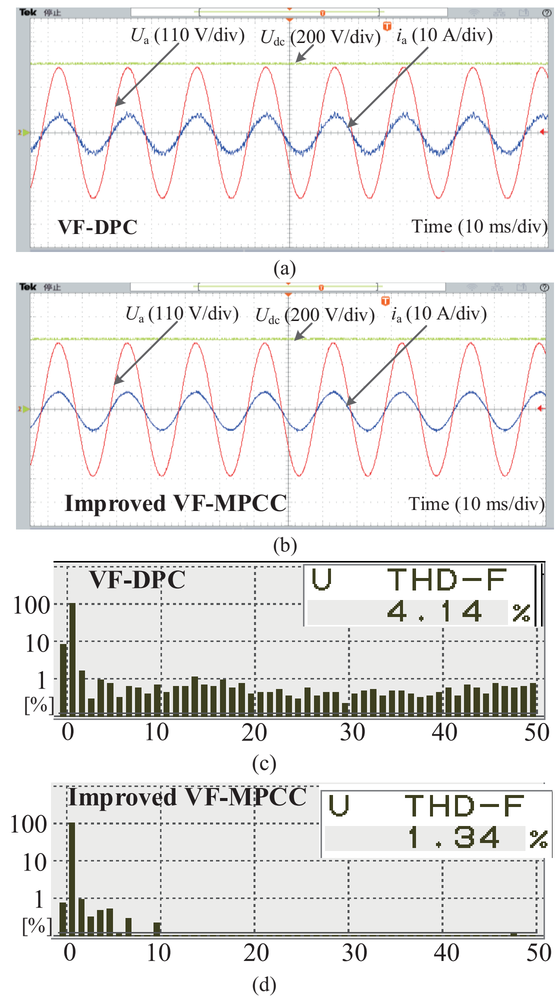

Fig. 6. Experimental results with VF-DPC and VF-MPCC under steady-state. (a) Phase-A voltage (U_a), Phase-A current (i_a) and DC-link voltage (U_{dc}) with VF-DPC. (b) Phase-A voltage (U_a), Phase-A current (i_a) and DC-link voltage (U_{dc}) with improved VF-MPCC. (c) THD of phase-A current with VF-DPC. (d) THD of phase-A current with improved VF-MPCC.

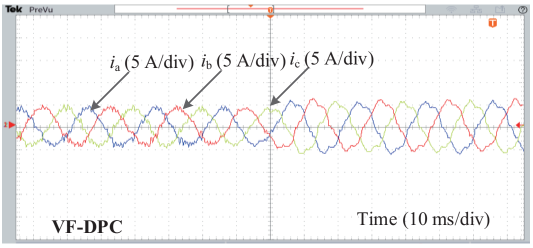

(a)

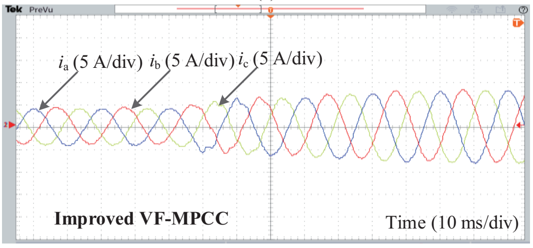

(b)

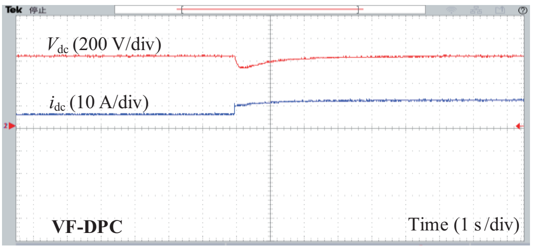

(c)

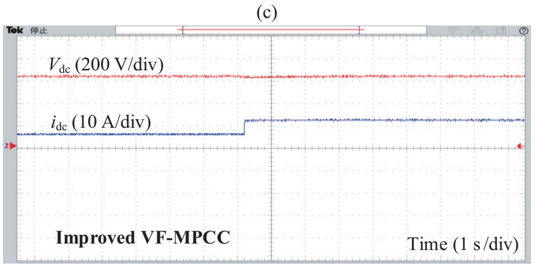

(d)

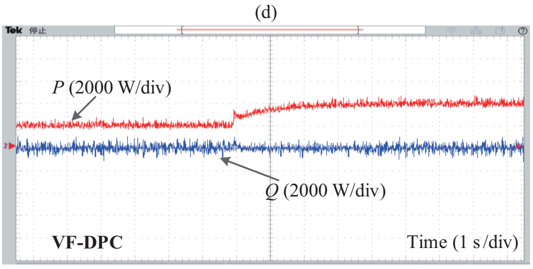

(e)

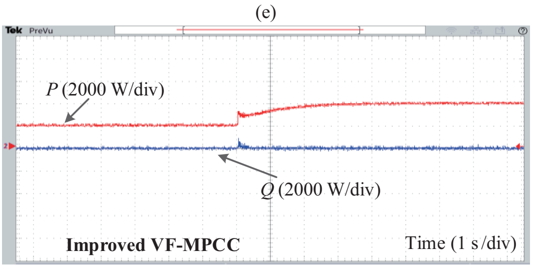

(f)

Fig. 7. Dynamic experimental waveforms with VF-DPC and improved VF-MPCC under variable load. (a) Three-phase current with VF-DPC. (b) Three-phase current with improved VF-MPCC. (c) DC-link voltage (V_{dc}) and current (i_{dc}) waveforms with VF-DPC. (d) DC-link voltage (V_{dc}) and current (i_{dc}) with improved VF-MPCC. (e) Active and reactive power waveforms with VF-DPC. (f) Active and reactive power waveforms with improved VF-MPCC.

Fig. 7 shows dynamic experimental waveforms with VF-DPC and improved VF-MPCC under variable load from half load to full load. Fig. 7(a) presents three-phase dynamic current waveform with VF-DPC. Fig. 7(b) shows three-phase dynamic current waveform with improved VF-MPCC. From Fig. 7(a) and (b), it can be seen that the dynamic response of the grid current is faster under the improved VF-MPCC strategy. The DC-side output voltage and current waveforms with VF-DPC are shown in Fig. 7(c). The DC-side output voltage and current waveforms with improved VF-MPCC are shown in Fig. 7(d). Compared with VF-DPC, in the proposed VF-MPCC strategy, the DC-side voltage drop is smaller during variable load, and the dynamic response time is shorter. Fig. 7(e) presents the waveforms of the active power and reactive power with VF-DPC control, in which, the power ripple is large. Fig. 7(f) presents the waveforms of the active power and reactive power with improved VF-MPCC, in which, the power ripple is very small. Therefore, the proposed VF-MPCC has a strong ability to suppress perturbations.

The waveforms of AC-side line-voltage and estimated voltage without voltage sensorless are shown in Fig. 8, respectively. AC-side line-voltage waveform of phase-AB estimated with VF-DPC is shown in Fig. 8(a). AC-side line- voltage waveform of phase-AB estimated with improved VF-MPCC is shown in Fig. 8(b). From Fig. 8(a) and (b), it can be seen that the line -voltage waveform with the proposed VF-MPCC has less disturbance and harmonics than that with VF-DPC. The grid voltage and the output of the voltage observer with VF-DPC are presented in Fig. 8(c), in which, it can be seen that there is a significant error between the phase-A voltage estimated (U_{ea}) by the voltage observer and the actual grid voltage (U_a). The grid voltage and the voltage estimated by the voltage observer with improved VF-MPCC are shown in Fig. 8(d). From Fig. 8(d), it can be seen that the estimated voltage and actual grid voltage are basically complete overlapping, and the proposed strategy effectively improves the prediction accuracy of the whole system.

The power factor with VF-MPCC and improved VF-DPC at different operating power is displayed in Fig. 9. From Fig. 9, the system power factor is almost maintained at 0.9999 with the proposed VF-MPCC.

The comparison between the VF-DPC and the improved VF-MPCC is presented in Table II. From Table II, it can be seen that the current THD and power factor of the steady-state, and the dynamic response time of the three-phase PWM rectifier are effectively improved under the proposed VF-MPCC.

Furthermore, in weak grid condition, the system stability is verified under VF-DPC and improved VF-MPCC, as shown in Fig. 10. Fig. 10 presents the experimental waveforms at SCR (short circuit ratio) = 1.5 (corresponding to L_m = 22 mH) and SCR = 1 (corresponding to L_m = 33 mH), respectively. While SCR = 1.5, the waveforms of the estimated voltage (U_{ea}), input current and the actual grid voltage (U_a) of phase A under VF-DPC and improved VF-MPCC are presented in Fig. 10(a) and (b). From Fig. 10(a) and (b), it can be seen that, under two control methods, the actual grid voltages have large disturbance,

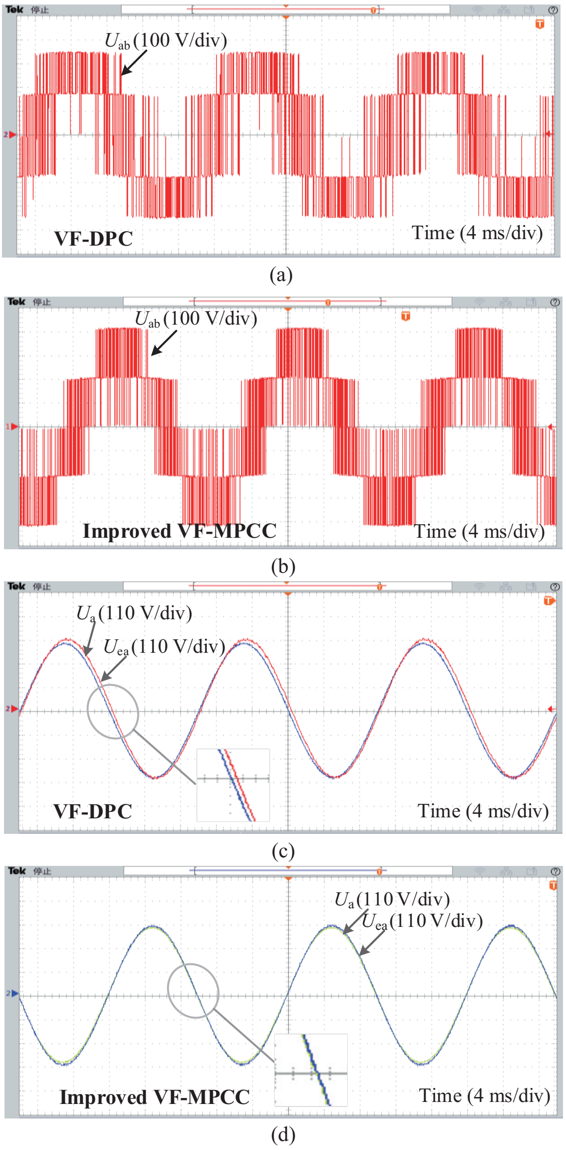

Fig. 8. Grid-voltage sensorless algorithm verification waveforms. (a) Estimated line-voltage (U_{ab}) on the AC side with VF-DPC. (b) Estimated line-voltage (U_{ab}) on the AC side with VF-MPCC. (c) Grid voltage (U_a) and voltage observer output (U_{ea}) waveforms with VF-DPC. (d) Grid voltage (U_a) and voltage observer output (U_{ea}) waveforms with improved VF-MPCC.

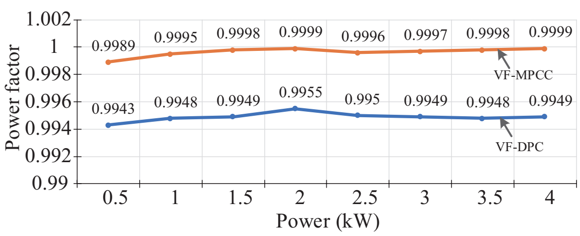

Fig. 9. The power factor with VF-MPCC and VF-DPC under different power.

TABLE II
QUANTITATIVE COMPARISON BETWEEN VF-DPC AND VF-MPCC

Evaluated parameters	VF-DPC	VF-MPCC
Steady-state current THD	4.14%	1.34%
Steady state power factor	0.9947	0.9999
Variable-load response time	1 s	0.25 s
Output voltage steady-state error	±0.20 V	±0.15 V

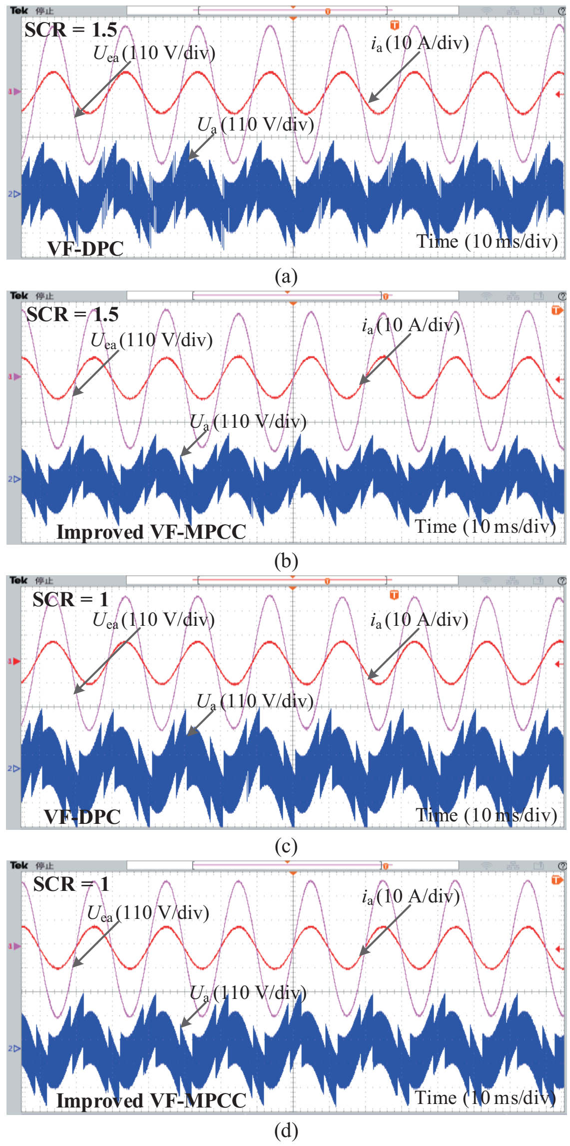

Fig. 10. Experimental results with VF-DPC and VF-MPCC in weak grid condition. (a) Phase-A voltage (U_a), Phase-A current (i_a) and Phase-A estimated voltage (U_{ea}) with VF-DPC at SCR = 1.5. (b) Phase-A voltage (U_a), Phase-A current (i_a) and Phase-A estimated voltage (U_{ea}) with improved VF-MPCC at SCR = 1.5. (c) Phase-A voltage (U_a), Phase-A current (i_a) and Phase-A estimated voltage (U_{ea}) with VF-DPC at SCR = 1. (d) Phase-A voltage (U_a), Phase-A current (i_a) and Phase-A estimated voltage (U_{ea}) with VF-MPCC at SCR = 1.

the estimated voltages and input currents are basically in phase. While SCR = 1, the wavefroms are shown in Fig. 10(c) and (d). It can be found that the actual grid voltages has greater disturbance than that with SCR = 1.5, the estimated voltages and input currents still remain same phase. Therefore, under the control strategy without grid-side voltage sensors independent of grid-side voltage information, the stability of the system is effectively improved in weak grid condition.

V. Conclusion

This paper proposes an improved VF-MPCC with bandstop filter feedback. The bandstop filter is used to suppress the dc component of the virtual flux observer, which is more accurate than the conventional calculation based on the pure integral. Based on the Lagrange interpolation method, the error of voltage vector selection in the two-step prediction algorithm is compensated. The proposed improved VF-MPCC is compared with the previous VF-DPC from steady-state performance, dynamic response, and voltage prediction accuracy. The experimental results show that, the improved VF-MPCC has good steady-state and dynamic performance, low current THD, high prediction accuracy under the same sampling frequency and presents high stability in weak grid condition. Hence, the improved VF-MPCC for PWM rectifier without grid-voltage sensorless is one of the optimal solutions to reduce hardware costs and improve system performance.

References

[1] A. Rahoui, A. Bechouche, H. Seddiki, and D. O. Abdeslam, "Grid voltages estimation for three-phase PWM rectifiers control without AC voltage sensors," in *IEEE Transactions on Power Electronics*, vol. 33, no. 1, pp. 859–875, Jan. 2018.

[2] F. Zidani, D. Diallo, M. E. H. Benbouzid, and E. Berthelot, "Diagnosis of speed sensor failure in induction motor drive," in *Proceedings of 2007 IEEE International Electric Machines & Drives Conference*, Antalya, Turkey, 2007, pp. 1680–1684.

[3] K. Jing, C. Liu, and X. Lin, "Discrete dynamical predictive control on current vector for three-phase PWM rectifier," in *Journal of Electrical Engineering & Technology*, vol. 16, no. 7, pp. 267–276, Jan. 2021.

[4] R. -J. Wai and Y. Yang, "Design of backstepping direct power control for three-phase PWM rectifier," in *IEEE Transactions on Industry Applications*, vol. 55, no. 3, pp. 3160–3173, May–Jun. 2019.

[5] O. Abdel-Rahim and H. Wang, "A new high gain DC-DC converter with model-predictive-control based MPPT technique for photovoltaic systems," in *CPSS Transactions on Power Electronics and Applications*, vol. 5, no. 2, pp. 191–200, Jun. 2020.

[6] X. Xiao, Y. Zhang, J. Wang, and H. Du, "An improved model predictive control scheme for the PWM rectifier-inverter system based on power-balancing mechanism," in *IEEE Transactions on Industrial Electronics*, vol. 63, no. 8, pp. 5197–5208, Aug. 2016.

[7] P. CortÉs, J. RodrÍguez, P. Antoniewicz, and M. Kazmierkowski, "Direct power control of an AFE using predictive control," in *IEEE Transactions on Power Electronics*, vol. 23, no. 5, pp. 2516–2523, Sept. 2008.

[8] A. M. Bozorgi, H. Gholami-Khesht, M. Farasat, S. Mehraeen, and M. Monfared, "Model predictive direct power control of three-phase grid-connected converters with fuzzy-based duty cycle modulation," in *IEEE Transactions on Industry Applications*, vol. 54, no. 5, pp. 4875–4885, Sept.–Oct. 2018.

[9] Y. Zhang, Y. Peng, and C. Qu, "Model predictive control and direct power control for PWM rectifiers with active power ripple minimization," in *IEEE Transactions on Industry Applications*, vol. 52, no. 6, pp. 4909–4918, Nov.–Dec. 2016.

[10] S. Yan, "An improved two-vector predictive direct power control using extended reactive power," in *Proceedings of 2020 IEEE 9th International Power Electronics and Motion Control Conference (IPEMC2020-ECCE)*, Nanjing, China, 2020, pp. 3166–3173.

[11] T. Na, X. Yuan, J. Tang, and Q. Zhang, "A review of on-board integrated electric vehicles charger and a new single-phase integrated charger," in *CPSS Transactions on Power Electronics and Applications*, vol. 4, no. 4, pp. 288–298, Dec. 2019.

[12] B. Hu, L. Kang, J. Liu, J. Zeng, S. Wang, and Z. Zhang, "Model pedictive direct power control with fixed switching frequency and computational amount reduction," in *IEEE Journal of Emerging and Selected Topics in Power Electronics*, vol. 7, no. 2, pp. 956–966, Jun. 2019.

[13] X. Wang, X. Liu, Z. Mo, J. Wen, and B. Xia, "Novel model predictive direct power control strategy for grid-connected three-level inverters," in *IET Power Electronics*, vol. 13, no. 16, pp. 3727–3733, Oct. 2020.

[14] S. Yan, Y. Yang, S. Y. Hui, and F. Blaabjerg, "A review on direct power control of pulsewidth modulation converters," in *IEEE Transactions on Power Electronics*, vol. 36, no. 10, pp. 11984–12007, Oct. 2021.

[15] K. Y. Tao, Q. Wu, L. Wang, and W. Tang, "Voltage sensorless predictive direct power control of three-phase PWM converters," in *IET Power Electronics*, vol. 9, no. 5, pp. 1009–1018, Apr. 2016.

[16] J. G. Norniella, M. J. Cano, and A. G. Orcajo, "Analytic and iterative algorithms for online estimation of coupling inductance in direct power control of three-phase active rectifiers," in *IEEE Transactions on Power Electronics*, vol. 26, no. 11, pp. 3298–3307, Nov. 2011.

[17] Y. Cho and K. -B. Lee, "Virtual-flux-based predictive direct power control of three-phase PWM rectifiers with fast dynamic response," in *IEEE Transactions on Power Electronics*, vol. 31, no. 4, pp. 3348–3359, Apr. 2016.

[18] J. -C. Kim and S. Kwak, "Model predictive virtual flux control to improve performance under distorted input voltage conditions," in *IEEE Access*, vol. 6, pp. 34921–34933, Jun. 2018.

[19] A. M. Razali, M. A. Rahman, G. George, and N. A. Rahim, "Analysis and design of new switching lookup table for virtual flux direct power control of grid-connected three-phase PWM AC-DC converter," in *IEEE Transactions on Industry Applications*, vol. 51, no. 2, pp. 1189–1200, Mar.–Apr. 2015.

[20] A. Jabbarnejad, S. Vaez-Zadeh, and M. Khalilzadeh, "Virtual-flux-based DPC of grid connected converters with fast dynamic and high power quality," in *Proceedings of IECON 2019 - 45th Annual Conference of the IEEE Industrial Electronics Society*, Lisbon, Portugal, 2019, pp. 4031–4036.

[21] H. Shi, X. Rong, P. Tuo, Y. Yao, and Z. Gong, "Model predictive direct power control for virtual-flux-based VSR with optimal switching sequence," in *IEEE Access*, vol. 10, pp. 38272–38283, Mar. 2022.

[22] Y. K. Tao, Q. H. Wu, W. H. Tang, and L. Wang, "Voltage sensorless predictive direct power control for renewable energy integration under grid fault conditions," in *Proceedings of 2015 IEEE Innovative Smart Grid Technologies - Asia (ISGT ASIA)*, Bangkok, Thailand, 2015, pp. 1–5.

[23] S. Djabali, M. A. H. Ali, and A. Ammar, "Improved virtual flux-direct power control for PWM rectifier based on second-order generalized integrators," in *Proceedings of 2020 International Conference on Electrical Engineering (ICEE)*, Istanbul, Turkey, 2020, pp. 1–6.

[24] Y. Zhang, Z. Wang, J. Jiao, and J. Liu, "Grid-voltage sensorless model predictive control of three-phase PWM rectifier under unbalanced and distorted grid voltages," in *IEEE Transactions on Power Electronics*, vol. 35, no. 8, pp. 8663–8672, Aug. 2020.

[25] S. Djabali, M. A. H. Ali, and A. Ammar, "Voltage sensorless direct power control for PWM rectifier under distorted network using improved virtual flux estimator," in *Algerian Journal of Signals and Systems*, vol. 6, no. 1, pp. 32–40, Mar. 2021.

[26] H. Li, M. Lin, M. Yin, J. Ai, and W. Le, "Three-vector-based low-complexity model predictive direct power control strategy for PWM rectifier without voltage sensors," in *IEEE Journal of Emerging and Selected Topics in Power Electronics*, vol. 7, no. 1, pp. 240–251, Mar. 2019.

[27] H. Zhang, X. Zhu, J. Shi, L. Tan, C. Zhang, and K. Hu, "Study on PWM rectifier without grid voltage sensor based on virtual flux delay compensation algorithm," in *IEEE Transactions on Power Electronics*, vol. 34, no. 1, pp. 849–862, Jan. 2019.

[28] C. Dang, F. Wang, X. Tong, D. Liu, X. Mu, and W. Song, "An improved voltage sensorless model predictive direct power control for Vienna rectifier," in *Proceedings of 2021 IEEE 1st International Power Electronics and Application Symposium (PEAS)*, Shanghai, China, 2021, pp. 1–6.

[29] R. Zhang, T. Hao, and C. Jia, "On-line monitoring of filter inductance suitable for voltage sensor-less direct power control," in *Proceedings of*

2020 IEEE/IAS Industrial and Commercial Power System Asia (I&CPS Asia), Weihai, China, 2020, pp. 1309–1314.

[30] M. Malinowski, M. Jasinski, and M. P. Kazmierkowski, "Simple direct power control of three-phase PWM rectifier using space-vector modulation (DPC-SVM)," in *IEEE Transactions on Industrial Electronics*, vol. 51, no. 2, pp. 447–454, Apr. 2004.

Chunjie Li received her B.S. and M.S. degrees in Electrical Engineering from the Shandong University of Science and Technology, Qingdao, China, in 2008 and 2011, respectively. She received her Ph.D. degree in Power Electronics and Electrical Drives from the Nanjing University of Aeronautics and Astronautics, Nanjing, China, in 2016.

In 2016, she joined the faculty of the College of Electrical Engineering and Automation, Jiangsu Normal University, Xuzhou, China, where she is presently working as a Lecturer. Since 2021, she has been an Associate Professor. Her current research interests include power electronics and the control of electrical machine drive systems.

Jianing Hu received the B.S. degree in Electrical Engineering from the Hebei University of Engineering, Handan, China, in 2021. He has been working toward the M.S. degree at Jiangsu Normal University, Xuzhou, China, since 2021. He specializes in the research field of power electronics applications.

Mingwei Zhao received the B.S. degree in mechanical and electrical integration from Nanjing University of Science and Technology, China, in 2004, M.S. degrees in power electronics and power drive from Nanjing University of Aeronautics and Astronautics, China, in 2012, and is currently working towards the Ph.D. degree in control Science and engineering, Shanghai University, China, in 2016.

He is also a Lecturer with the School of Electrical Engineering and Automation, Jiangsu Normal University, Xuzhou, China. His research interests include new power electronics drive technology and robot system.